PAPER • **OPEN ACCESS**

3D printed PCL-nHAp composite implants for the treatment of segmental bone defects: *in vivo* application in a rabbit model

To cite this article: D Basoz *et al* 2025 *Biofabrication* **17** 015041

Biofabrication

PAPER

3D printed PCL-nHAp composite implants for the treatment of segmental bone defects: *in vivo* application in a rabbit model

D Basoz[1,2], **M I Karaman**[3], **S Buyuksungur**[4], **D Yucel**[1,2,5], **N Hasirci**[4,6,7,†], **B Kocaoglu**[1,2,3] and **V Hasirci**[1,2,4,8,*]

[1] Graduate Department of Biomaterials, Acibadem - University, Istanbul, Turkey
[2] A Biomaterials Research and Application Center, Acibadem University, Istanbul, Turkey
[3] School of Medicine, Department of Orthopedics and Traumatology, Acıbadem University, Istanbul, Turkey
[4] Middle East Technical University, BIOMATEN, Center of Excellence in Biomaterials and Tissue Engineering, Ankara, Turkey
[5] School of Medicine, Department of Histology and Embryology, Acibadem University, Istanbul, Turkey
[6] Department of Chemistry, Middle East Technical University, Ankara, Turkey
[7] Department of Bioengineering, Near East University, TRNC, Mersin, Turkey
[8] Department of Biomedical Engineering, Acıbadem University, Istanbul, Turkey
[*] Author to whom any correspondence should be addressed.
[†] Publisher's note. Whilst IOP Publishing adheres to and respects UN resolutions regarding the designations of territories (available at www.un.org/press/en), the policy of IOP Publishing is to use the affiliations provided by its authors on its published articles.

E-mail: vasif.hasirci@acibadem.edu.tr

Keywords: segmental bone defect, biodegradable, poly(ε-caprolactone), hydroxyapatite, 3D print, composite implant

Supplementary material for this article is available online

OPEN ACCESS

RECEIVED
27 May 2024

REVISED
5 December 2024

ACCEPTED FOR PUBLICATION
16 December 2024

PUBLISHED
30 December 2024

Abstract

The management and treatment of long bone defects are challenging clinical problems. In this study, in order to address the need for load bearing implants for segmental defects, 3D printed cylindrical implants of poly(caprolactone) (PCL) and nanohydroxyapatite (nHAp) composites were prepared and applied as lateral segments to the femurs of New Zealand white rabbits. The results of PCL-nHAp implant group obtained 6 weeks after the procedure were compared with those of the autografts. There was no significant difference between the yield and ultimate loads of autograft group and the implant group. Histological studies demonstrated similar new bone formation in both groups. Also, a sizeable callus formation around the autografts and bone ingrowth to the 3D printed implants were observed, and x-ray studies confirmed the formation of the callus. An increase was detected in the bone density around the defect site for both test groups. SEM revealed close interaction between the newly formed bone tissue and the struts of the 3D printed implant. mRUST values, which is an indicator of tissue healing, increased continuously during 6 weeks. In conclusion, 3D printed, 1.5 cm long cylindrical nHAp-PCL implants exhibited excellent bone healing and biomechanical stability in the large lateral segmental bone defects of the rabbits even in a relatively short implantation time as 6 weeks. We believe that these implants could serve as an alternative to autografts in the treatment of long bone defects.

1. Introduction

Segmental bone loss caused by trauma, tumor resection or diseases is a challenging problem to manage, because they cannot heal by themselves, require long treatment durations, and application of difficult techniques, which are sometimes very uncomfortable for the patients [1]. Segmental bone defects are preferentially treated with autografting by using the patients' own bone tissue, which is accepted as the gold standard [2, 3]. Contemporary applications include, induced membrane techniques, distraction osteogenesis, primary shortening, Vascularized Fibular Graft transfer [3, 4] In severe cases, the solution is amputation. Some of these techniques, use autologous bone graft, allograft, or bone substitutes, while others use various materials such as metals, ceramics, polymers, decellularized tissues or composites of several of these

[5]. A large number of implants are needed, due to the scarcity of the autografts [6–9].

In the early years, metals were the materials of choice because of their mechanical strength, and absence of other materials but then new, highly biocompatible and durable implants were produced from polymers and their composites with ceramics and metals to substitute for metals [10]. In the literature, there are now a large number of preclinical and clinical studies, involving biodegradable ceramics (e.g. calcium sulfates, hydroxyapatite (Hap), tricalcium phosphate (TCP), etc) and polymers in the treatment of such bone defects [11–18].

HAp, which is a naturally occurring calcium phosphate that exists in bone structure, is the most commonly used ceramic in the preparation of osteoinductive implants. It is either used alone or in combination with other calcium phosphates such as TCP and polymers. Different types of CaP-based materials used in bone repair are reported in the literature [19, 20]. Bansal *et al* examined the suitability of a mixture of HAp and β-TCP as a periodontal graft material in the treatment of intrabony three-wall defects and reported significant pocket depth reduction and clinical attachment gain [21]. There are also studies carried out with various combinations of 3D-printed bone grafts of HAp and TCP for use filling defects in animal models [22, 23]. In one case, scaffolds made of HAp were loaded with bone marrow stem cells (BMSC) exosomes and used under hypoxic conditions to repair calvarial defects in rats and were found to promote angiogenesis and osteogenesis [22] .In another study, biphasic calcium phosphate containing 30% HAp was prepared in the shape of a hollow cylinder by molding and sintering. It was used as a segmental implant, secured in place with intramedullary nail fixation and successfully used in the treatment of goat femur defects [24]. Although the regenerative efficacy of the HAp and TCPs are very promising, there are some constrains in their production as patient specific devices [25]. This is due to the difficulty of production of these implants with patient specific interior and exterior architecture, controlled porosity and interconnectivity, and not with the size and geometry to perfectly fit the defect shape which are all required for proper contact with the neighboring natural tissue [26]. Therefore, composites of CaPs, including HAp, are generally prepared by mixing them with polymers to satisfy all those requirements [27–29].

In the production of bone implants, there are a wide variety of biocompatible and biodegradable polymers approved to be suitable for medical use such as poly(ε-caprolactone) (, polylactides and their copolymers like poly(lactide-co-glycolide)s with various compositions, poly(-hydroxybutyrates), etc, the properties of which can be optimized to a large extent to suit the targeted use [30]. Their mechanical properties, stability, and interaction with cells can be adjusted using a number of chemical processes and also by blending with other polymers or ceramics [31, 32].

Poly(caprolactone) (PCL), is one such polymer which was approved by the United States Food and Drug Administration for use in clinical applications. It is degradable by hydrolysis at a rate determined by its crystallinity, molecular weight, and the design (e.g. thickness, porosity) of the product. It is, used frequently in biomedical applications including bone repair due to its required mechanical strength [33–39]. The rate of degradation of PCL is comparatively slow and complete degradation takes between months to 2–4 yrs depending on the molecular weight, crystallinity, and design of the implant [40]. Therefore, its composites with CaPs are preferable to both enhance its degradation rate and biocompatibility, and also its mechanical strength. Over the years, blends of ceramics with PCL were used in a variety of *in vitro* and *in vivo* tests [41, 42]. In one study, nanocomposites of PCL granules and hydroxyapatite in cylindrical form (Dia 6 mm, length 5 mm) tested on the New Zealand white rabbits in the regeneration of femoral bone defects [43]. The results showed that on day 45 postop, the quantity of newly formed lamellar bone in the healing site in PCL group was better compared to pure HAp group [43].

In many studies PCL implants are being produced by three-dimensional printing (3DP), especially with fused deposition approach for which the low melting point (55 °C–60 °C) of PCL is very convenient. Its strength and flexibility, appropriate rheological and viscoelastic properties, and the low melting point (55 °C–60 °C) are its main advantages [44, 45]. The 3D printing technique is a useful tool for production of scaffolds with the required features such as proper geometry and microarchitecture. The implants are built using the data obtained from microCT or MR images of the defect site on the patient, and therefore, the product obtained is specific for the patient. 3D-printed PCL-based composite scaffolds prepared in different forms for bone tissue engineering applications was summarized by Gharibshahian *et al* [35]. In this review article, the advantages of 3D printing as well as healing efficiency of the PCL based composites having bioactive compounds (e.g. drugs, growth factors, cells) with their osteoinduction, osteoconduction and osteointegration properties were covered. Park *et al* 3D printed, patient-specific PCL/ ß-TCP implants for use in the cranioplasty of seven patients, and reported rapid and appropriate healing after six months [46].

Implants prepared from PCL and TCPs were successfully used in dentistry and cranioplasty, but their applications in the treatment of large and load-carrying bone defects are limited. Mayfield *et al*

reviewed the current strategies for management of segmental bone loss in orthopaedic surgery, including graft selection, bone graft substitutes, and operative techniques, with 3D printed PCL implants in general, where in some cases BMSC were added to the strucutres [37, 47].

Some of the *in vivo* orthopedic tests involved segmental application, but mostly the implants were in the form of buttons and tested either subcutaneously or placed on the femoral side wall as was also used in some of our previous studies [34]. In this study, a circular defect (dia of 5 mm) was drilled in the shaft of the femur and the 3DP implant was used to fill the hole. The results showed that the implant almost filled the defect site in 8 weeks while the defect free control did not. The main problem with such studies is that, the need for segmental defects in the real clinical setting is more than circular defects. Besides, the side wall button implants do not carry any load or contact the bone marrow, and therefore do not mimic the real situation [48].

Popkov *et al*, in 2023, prepared 3D printed, PCL implants coated with HAp and investigated osseointegration 20 mm long segmental tibial defects in sheep. Stainless steel rings, Kirschner wires and an external frame was used in the fixation of the implant. They reported that at 4 weeks post-op the pores of the implant were completely filled with the newly formed bone tissue [49].

In the present study, because of the need for a strong, load bearing structure, and a design which allows tissue ingrowth, a cylindrical implant of nanohydroxyapatite (nHAp) and PCL blend was printed for segmental application in bone defect cases with the aim of investigating the healing potential of 3DP a nHAp-PCL composite implant in the treatment of segmental femoral bone defects. The control was an inverted femur segment of another rabbit. The hypothesis of the study was that nHAp PCL implants prepared via 3DP approach will achieve bone healing and biomechanical stability similar to that of the autogenic bone graft in the treatment of segmental femoral bone defects and thus decrease the demand for autografts or non-degradable implants.

2. Materials and methods

Poly(ε-caprolactone) (PCL; MW of 50 kDa) and nHAp (<200 nm) which were used as the main materials of the implants were obtained from Polysciences (USA) and Sigma Aldrich (USA), respectively. The Shandon TBD-2 Decalcifier solution used for histological analysis was purchased from Fisher Scientific (USA). The neutral-buffered formalin solution, phosphotungstic acid hydrate, phosphomolybdic acid hydrate, acetic acid, and aniline blue solution were obtained from Sigma-Aldrich (USA). Hematoxylin solution was product of J.T. Baker Chemical Co. Eosin was purchased from Biyosistem Medikal Ltd and Weigert's Iron Hematoxylin solution was purchased from Merck Millipore Co.

Purity of nHAp was determined at METU Central Laboratory using x-ray diffraction analysis under the conditions: Duration/Scan speed: 1 deg min^{-1}, Step/Sampling step: 0.02 deg, Measurement axis: 2Theta and Scan range: 3–90 deg. The information obtained can be summarized as: Phase Name: Hydroxyl apatite, Formula: Ca 10.084, PO_4: 5.94 (Figure of Merit: 0.3256840130410147, Space Group 176: P63/m). This data indicated that the HAp used in the study was pure, consisted of a single phase and the Ca:P ratio of the material was 1.70, proving the purity of HAp (supplementary figure S1).

2.1. Preparation of 3D printed PCL with nHAp

The PCL-nHAp implants were 3D printed in cylindrical form by fused deposition modeling technique using EnvisionTEC printer (Gladbeck, Germany). The implant (diameter: 10 mm, height: 15 mm, 47 layers) was printed with each layer shifted 0.15 mm with respect to the previous layer oriented in the same direction (2 layers up or down). The polymer powder was blended with %10 (w/w) nHAp. Printing conditions were: Fiber orientation between layers: 0–90, shifting in each layer 0.15 mm, needle inner diameter: 400 μm (22 G), distance between fibers: 1.2 mm, and printing temperature: 160 °C. After 3D printing, the implants were soaked in 70% ethanol (EtOH) for 2 h for sterilization for the *in vivo* studies. Following the ethanol treatment, the implants were air-dried overnight in a biosafety cabinet.

2.2. Characterization of PCL-nHAp implants

Morphological Analysis: Morphological analysis of the 3D printed PCL-nHAp scaffolds was achieved with a Scanning Electron Microscope (SEM; Zeiss EVO-10, Germany) after sputter coating with gold under vacuum. Fiber diameter and the pore size of the implants were measured by Image J using SEM micrographs. The printed model is presented in figure 1(A).

Porosity: A pycnometric approach was used to determine the porosity of the 3D printed PLC-nHAp scaffolds using the equation given below;

$$\text{Porosity } (\%) = (V_a/V_s)\ x\ 100$$

where V_a is the void volume in the scaffold *and* V_s = *Volume of the* 3D printed scaffold calculated from external dimensions

Dispersion of nHAp in the implant: The samples were scanned with a MicroCT scanner (Skyscan 1175, Germany) in order to check the dispersion of nHAp particles in the polymer. The scanning parameters were 60 kV, 125 μA, 13 μm/pixel, using 1 mm Al filter.

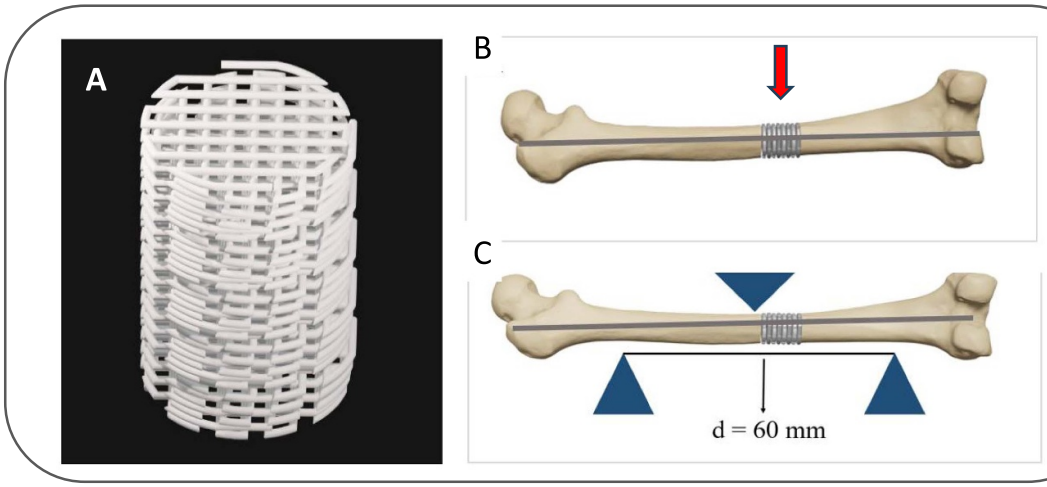

Figure 1. PCL-nHAp implants. (A) Design of the implant, (B) schematic presentation of the segmental placement of the implant (arrow shows the implant site), (C) the testing scheme of the femurs with 3-point bending set up.

Compression Test: The mechanical properties of the 3DP cylindrical scaffolds (10 mm diameter and 10 mm height) were studied with compression tests using a Mechanical Tester (Shimadzu AGS-X Universal Test Machine, Japan). The compression speed was 1 mm min^{-1}, 5kN cell load was used. The compressive modulus of the scaffolds was calculated from the initial linear elastic region of the stress–strain curves.

2.3. *In vivo* application of the PCL-nHAp implants

For *in vivo* experiments, 16 male New Zealand male white rabbits (28–30 weeks old, 3–4 kg) which were obtained from Acibadem University Animal Research Center, were used. In order to determine the required sample size for our study, we conducted a power analysis using IBM SPSS Statistics (Version 27.0.0.0). The analysis was based on the assumption that the mean value of one of the two groups to be compared is 1, while the mean value of the other group is 0.7. The standard deviation for both groups was estimated to be 0.20. We aimed for a power of 0.8 (80%) and set the significance level (alpha) at 0.05. This analysis was performed for a two-sample *t*-test, resulting in a calculated sample size (N) of 8.

Ethical approval was obtained for the use of laboratory animals by the Research Ethics Commission for animal experiments (ACU-HADYEK 2018/42). The animals were housed in a pathogen-free facility under optimal housing conditions: 25 °C, with 12 h light and 12 h dark cycle while being kept in a stress-free and isolated environment. The rabbits were divided into two groups by simple randomization. The animals were randomly divided into two groups: Group 1: Eight rabbits received 3DP PCL-HAp (10 mm diameter, 15 mm height) for segmental bone implantation (figure 1(B)). Group 2: Eight rabbits received their own 1 cm long autogenous segmental bones after being reversed in direction. The opposite heathy legs used as control.

All rabbits received a sedative (Carprofen 2.2 mg kg^{-1}, s.c.) followed by a long-term anesthetic application (ketamine 30 mg kg^{-1}; xylazine 5 mg kg^{-1}, i.m.). A longitudinal incision was made on the lateral side of the femur, tensor fascia lata was dissected to reveal the diaphysis. Periosteum was opened in distal and proximal directions and femoral shaft was exposed. In Group 1, cylindrical segmental bone (15 mm long) was excised from the central diaphysis to create a segmental defect where 15 mm long PCL-HAp implant was placed to the segmental gap and fixed with an intramedullary 1.2 mm K-wire as mimicking intramedullary nailing procedure in human clinical scenario (figure 1(B)). In Group 2, cylindrical segmental bone (1 cm long) was excised from the central diaphysis to create a segmental defect and same resected bone was reinserted to the segmental gap after reversing its direction and fixed with an intramedullary 1.2 mm Kirschner wire. After the closure of the surgical sites, lower extremity cast were applied to all rabbits to secure the operation area. A post-operative dose of intramuscular (i.m.) cefazolin sodium (0.1 mg kg^{-1} Cefozin, Bilim Ilac, Türkiye) was injected into all animals for infection prophylaxis. The rabbits were housed for 6 weeks without immobilization. During this period the state of the implant sites were studied radiologically at weeks 2, 4 and 6. All rabbits were sacrificed via an intrathoracic/intracardiac overdose injection of Pentobarbital (5 ml; 16 mg/100 ml). After that the femurs were removed. All groups were compared by radiological studies (x-ray, CT) in terms of radiological bone healing, by mechanical testing for strength and stability, and by histological analysis for bone healing levels and

the overall performance. *During the 6 week study, all samples/rabbits were subjected to x-ray imaging at 1, 3, and 6 weeks, and the results were used in the analyses.* After harvesting, groups of 8 rabbits, 3 samples from each group (implant, autograft, control) were set aside for histology studies and the remaining 5 samples of each group were subjected to radiological studies, followed by mechanical testing of 4 of them. The remaining 1 sample from each group was evaluated using SEM.

2.4. Mechanical testing with 3 point bending

Femurs were harvested after the rabbits were sacrificed and preserved in PBS at +4 °C without any fixation. Soft tissue on the femur around the implant site was removed by scraping. Femurs from each group (3DP PCL-HAp implant, autograft, and untreated control) were tested with Mechanical Testing Machine (Shimadzu AGS-X Series Universal Test Machine, Japan) in 3-point bending mode. The data was analyzed using Mechanical Testing Software (Trapezium, Shimadzu, Japan). Stress was applied at a rate of 1 mm s^{-1} (figure 1(C)). Force/strain curves were acquired (a representative example is presented in supplementary figure S2) and ultimate load and yield point values were calculated.

2.5. Histological analysis

Harvested bone samples were fixed in neutral formalin (%10, pH 7.0) and decalcified with Decalcifier-Shandon TBD-2 solution for 20 d. The decalcified bones were cut in longitudinal and cross-section directions and the samples were treated with a series of increasing concentrations of ethanol solutions (70%, 90%, 100% EtOH) for dehydration, and then placed into xylene before embedding in paraffin. Sections 5 μm thick were removed from the paraffin-embedded tissue, and deparaffinization and hydration were performed by applying xylene and decreasing alcohol series (100%, 90%, 70% EtOH), respectively. Sections were stained with Hematoxylin–Eosin (H&E) and with Masson's Trichrome, then examined with light microscope, and then evaluated in terms of tissue response to implant, bone-implant integration and new bone formation at the injury site.

2.6. Radiography studies

2.6.1. CT segmentation and volume analysis

After the rabbits were sacrificed, randomly selected 5 autograft specimens, 5 control specimens and 5 implant samples were examined by imaging with Siemens SOMATOM Force CT Scanner (Siemens AG, Munich, Germany) using lower extremity bone dosing. DICOM (Digital Imaging and Communications in Medicine) image resolution was 512 × 512 PPI and slice thickness was 0.5 mm. DICOM images were imported to MIMICS Research (Version 21.0.0.406) to create 3D reconstruction of samples and to perform volume measurements. Each sample was segmented between 226–1200 Hounsfield Unit and 3D reconstructed. In order to measure the volume of each sample in a reproducible manner, 2 incision polygons (thickness of 0.1 mm, 20 mm apart and parallel to each other) were placed in the distal and proximal femur fractures by centering a 15 mm long scaffold and autograft. In the control group, the same procedure was applied to the same anatomical region that was treated in the other groups. Volume was expressed as mm^3. After all of these, each group was compared by two-sample t-test analysis. The control group was the opposite, healthy leg of the same rabbit.

2.6.2. Radiographic union score in tibial fracture (RUST) for healing levels

After the surgical procedure was performed, anterior–posterior (AP) and lateral x-ray images of the implant sites were obtained with Siemens ARCADIS C-arm (Siemens AG, Munich, Germany) at week 1, 3 and 6 for 16 rabbits' lower extremity. In order to evaluate and classify healing levels of diaphyseal fractures of rabbit femur, a novel method, Radiographic Union Score in Tibial Fractures (RUST), that shows the presence or absence of fracture line and callus, was used [50–52]. In our study, we used modified RUST (mRUST) to distinguish differences along a relatively short term of observation (6 weeks) [51, 53]. mRUST, as explained by Litrenta *et al*., is performed using AP and lateral radiographs and assigns a score depending on the healing of four cortices of the bone [53]. The maximum score for RUST is 16 (bone healing is complete) while the minimum score is 4 (no healing) (table 1). In order to evaluate callus creation and whether there is bone healing, control x-ray was performed with AP and lateral projections at weeks 1, 3 and 6, covering both femurs of each rabbit. Data was examined and scored by two independent, blinded observers and evaluated in accordance with the average of the values the observers decided on. During the mRUST score comparison, only the implant and autograft groups were compared.

2.7. Statistical analysis

Statistical analysis was applied to the data obtained. For 3 point bending mechanical test, statistical analysis was performed using the R program, a free software used in statistical computing, to compare the results of 3-point bending mechanical tests. ANOVA test was used for two-to-many comparisons and the t-test was used for two independent samples between two groups. The p values less than 0.05 ($p < 0.05$) were considered statistically significant.

The mRUST scores, which were calculated according to the x-ray measurements performed on

Table 1. Modified radiographic union score table for tibial fractures (mRUST).

	Anterior cortex	Posterior cortex	Medial cortex	Lateral cortex	Total
(+) Fracture line, (−) Callus	1	1	1	1	Min 4
(+) Fracture line, (+) Callus	2	2	2	2	
(+) Fracture line, (+) Periosteal Bridging callus	3	3	3	3	
(−) Fracture line, (+) Remodeled Tissue	4	4	4	4	Max 16

weeks 1, 3 and 6, were examined by performing two-sample *t*-test between two groups in the same week. CT volume measurements were analyzed by performing two-sample *t*-test between control, scaffold and autograft group with %95 CI (Confidence Interval). Linear regression analysis was also performed for 2 groups to test mRUST according to time with %95 CI. Inter-rater reliability was assessed with intraclass correlation coefficient (ICC). Two-way random agreement type ICC to evaluate the mRUST scores of two observers with %95 CI. To interpret the ICC values, work of Landis *et al* [54] was considered. 0–0.2 was defined as slight agreement, 0.21–0.40 as fair agreement, 0.41–0.60 as moderate, 0.61–0.8 as substantial, and values 0.80 or higher to be in essentially perfect agreement for the ICC evaluations. IBM SPSS Statistic (Version 27.0.0.0) was used to calculate all above.

3. Results

3.1. Morphological and physical properties of the PCL-nHAp implants

Morphological and physical properties of the implants were examined with SEM and MicroCT analyses for the thickness of the struts, porosity, and dispersion of nHAp in the 3D printed structures.

Thickness of struts, pore size and porosity of 3D printed structures: According to SEM images, the struts of the 3D printed implant samples were uniform in thickness, and average diameter of the struts was found to be 404 ± 17 μm. The implant was designed to have a high porosity and large pore sizes, which were determined as 86 ± 1%, and 702 ± 2 μm, respectively (figures 2(A) and (B)). It is reported that chondrocytes and fibroblasts cultured on scaffolds preferred to proliferate in 400 μm pores and promoted osteoconductivity [55]. It was also reported that the highest seeding efficiency was obtained with pore sizes of around 500 μm [56]. In this study, the structures prepared had homogeneous, large pores in order to enhance cell attachment.

Dispersion of nHAp in the implant: MicroCT analysis revealed a uniform distribution of nHAp throughout the implant structure, with images indicating that all the struts of 3D printed PCL-nHAp scaffolds with homogeneous distribution of nHAp particles, (figures 2(C)–(E)).

3.2. Mechanical properties of the implants as determined by compression

Mechanical properties of the 3DP scaffolds were determined by application of compression. Also, 3-point bending tests were carried out on the implanted samples and healthy bone control group samples. Using the stress–strain curves obtained from compression tests, compressive moduli of the 3DP scaffolds were calculated as 33.3 ± 3.2 MPa.

3.3. Mechanical testing by 3-point bending

3-point bending tests on the samples were carried out after termination following implantation procedure, using health untreated leg bone as the control group. For these implanted samples, tests were performed on samples of bone attached to the implant material (e.g. PCL-HAp implants, autografts, and the untreated healthy control femurs). The results are presented in table 2 and figure 3

The yield point is the load at which the material loses its elasticity and will no longer return to its original form and becomes permanently deformed. The yield point of a material is therefore the point where transition between elastic and plastic deformation happens. The ultimate load, on the other hand, is the maximum load that material can resist before breaking. The results of the 3-point bending test indicate that the autograft and implant groups had significantly lower Ultimate Load and Yield Load values compared to the untreated healthy control group ($p < 0.05$), as expected. On the other hand, there was no significant difference between the yield

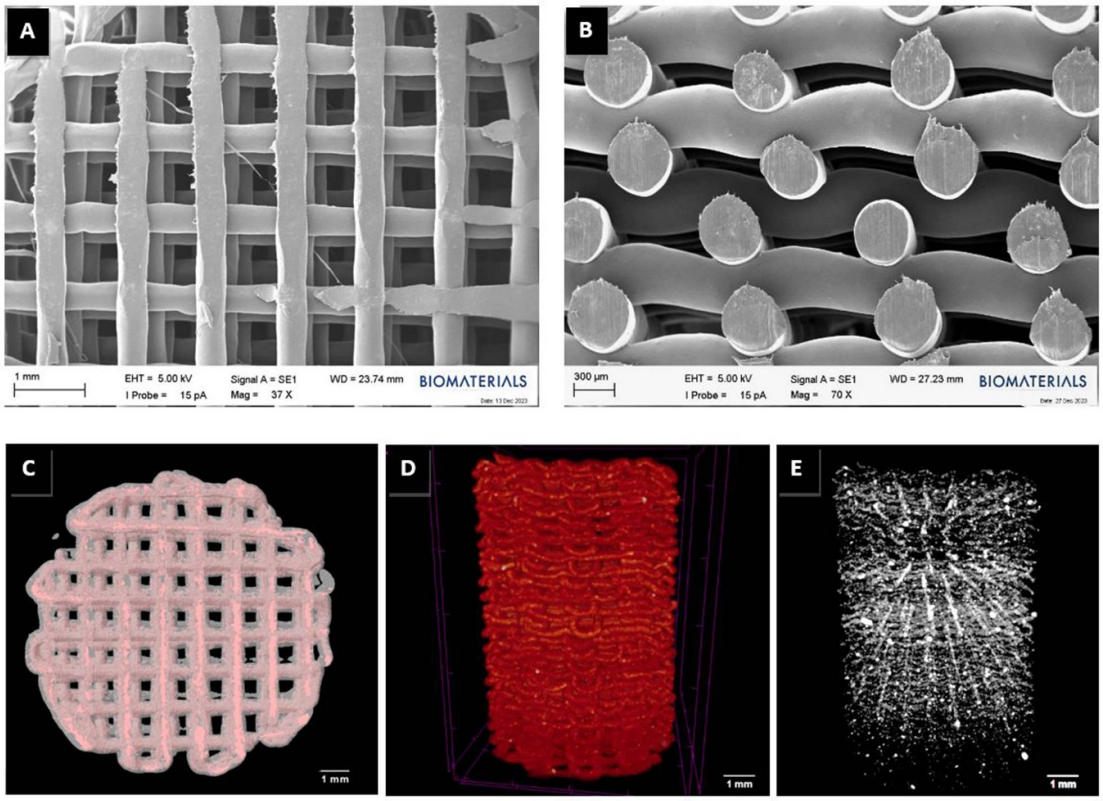

Figure 2. Micrographs of the 3DP PLC-nHAp implants. (A) SEM of top view, (B) SEM of side view (cut longitudinally), (C) micro-CT of top view; (D) micro-CT of side view; (E) micro-CT showing the distribution of the nHAp particles in the scaffolds.

Table 2. 3-Point bending mechanical test results of rabbit femurs (week 6).

	Ultimate Load (N)	Yield Load (N)
Control ($n = 4$)	245 ±5	203 ±29
Implant ($n = 2$)	57 ± 5	50 ± 1
Autograft ($n = 4$)	93 ± 56	47 ± 9

and ultimate loads of autograft group and implant group both types of implants ($p > 0.05$). Despite a 6 week period being relatively short for bone healing, both groups were able to withstand mechanical loading, suggesting some level of integration between the implant and the bone. This can be attributed to the fact that autografts consist of fully matured bone with intact extracellular matrix and cells at the time of reimplantation, giving them a significant advantage over the cell free and highly porous 3D printed implants. On the other hand, promising compatibility of the implant and the tissue gives hope about the material, shape and performance of the 3DP implant with patient specific shape and inner and exterior geometry.

3.4. SEM analysis of the implantation area

Femur bones of rabbits, harvested after 6 weeks of implantation, were examined with SEM (Thermo Quatro ESEM) under 'low vacuum mode' without coating. Scheme of the area of implantation (with a red box) and the actual implantation image are shown in figure 4.

SEM images (figures 4(C) and (D)) show that the implant and the new forming bone are highly integrated, the bone attaching tightly to the pores of the implant. The slight gaps at certain points are most probably due to drying process of the samples for SEM analysis. This shows that the implant material and bone are compatible and the interaction is acceptable. Another observation is the implant retains its form after 6 weeks indicating that the complete replacement of the implant by the bone needs a longer duration for a strong bone provides mechanical support at the defect site.

3.5. EDS analysis of the implantation area

The implants retrieved after termination of the rabbits were examined with the EDS accessory of the SEM (Thermo Scientific, Quattro SEM) in order

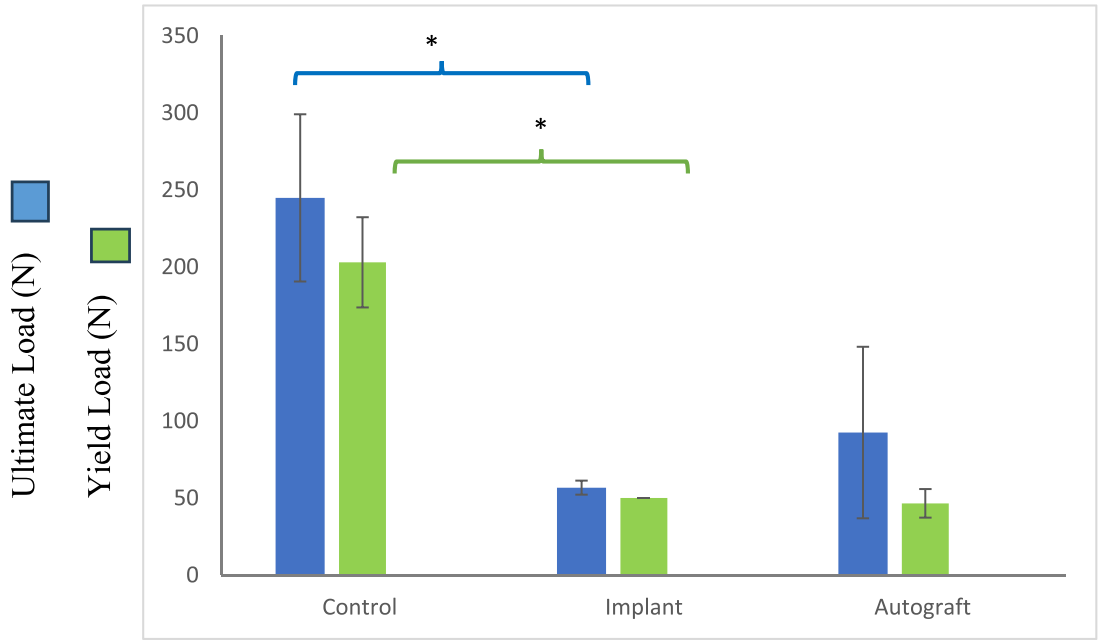

Figure 3. Mechanical properties (ultimate load and yield point load) obtained by 3-point bending test of the implants after 6 week of implantation. Control is untreated, healthy femur. Autograft is reversed femur segment. Implant is 3D printed PCL-HAp implant. (* p value < 0.05,).

to chemically characterize the implantation area consisting of the implant, femoral bone and the newly forming tissue on the implant. The EDS (obtained from the same site of the SEM) shows that on the implant side(s) carbon is dominant even though the added hydroxyapatite consists of calcium and phosphate due to its composition ($Ca_3(PO_4)_2$) (figures 4(E) and (F)). On the bone side, calcium and phosphorous are also present due to the native HAp of the cortical bone along with the carbon from the biological tissue such as collagen. Oxygen is present in both structures, and therefore, it is detected on both sides. What is not present among the components of the implant is nitrogen which is abundant in natural tissues and is indicated as pink in the bone side. These results are in agreement with the composition of the bone, which is basically HAp (a calcium phosphate with a formula of $Ca_{10}(PO_4)_6(OH)_2$) and the carbon-based chemistry of the natural tissue. In figures 4(G)and (H) the interface of the implant and the ingrown tissue is presented. The tight interaction between the ingrown tissue and the implant is clearly seen both in the SEM and the EDS.

3.6. Histological analysis

Histological studies were conducted to evaluate tissue repair and new bone formation after 6 weeks of implantation. Longitudinal and cross-section micrographs of the implant and autograft groups following Masson's trichrome and H&E staining are presented in figures 5 and 6, respectively. The intact, healthy bone structure with well-organized compact bone of the diaphysis region and the bone marrow in the medullary cavity were observed in the control (untreated healthy femurs) group (figure 5(b)). In histological results of both implant and autograft groups, new bone tissue formation was observed with the callus formation (figures 5 and 6). Stereomicrographs involving the whole tissue section, showed that in the implant groups new bone formation was mainly localized at the periphery of the scaffolds (figures 5(c) and (f)). Even the spaces between struts of the scaffolds were filled mainly with fibrous connective tissue, and it was seen clearly that there were occasional bone trabeculae formation within some spaces (figures 5(c), (e) and (f)). The newly formed bone and connective tissues between the struts were fragmented and removed during tissue processing. New bone formation at the periphery of the implant is prominent especially in the micrograph of the cross section (figure 5(f)). However, the native bone tissue-implant interface is clearly seen in the longitudinal section of the implant group (figure 5(c)). In both implant and autograft groups, it was observed that osteoblasts surrounded the newly formed trabeculae, and the osteocytes were integrated into these trabeculae (figures 5 and 6). In addition, osteoclasts were also observed around these trabeculae. In both longitudinal and cross sections of the implant, it was seen that thick bone spicules, and even trabeculae, developed and new bone tissue formation occurred by the fusion of these trabeculae

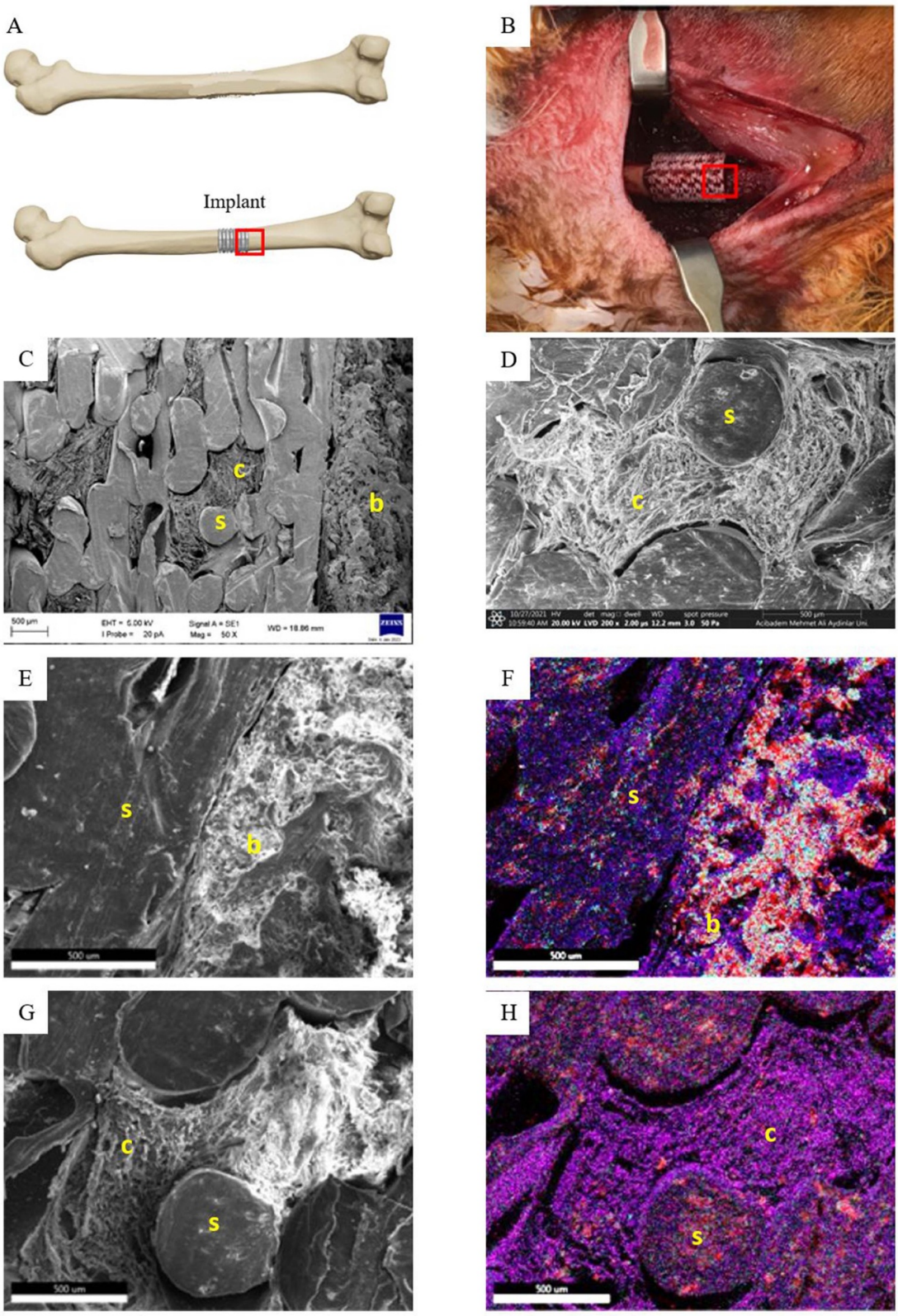

Figure 4. The location on the femur for implantation. (A) Scheme of implantation site, (B) The implant site on the rabbit femur. (C)–(D): SEM showing implant-femoral bone interface and ingrown callus. (C) Implant struts (s) are seen as circular, smooth forms. Femoral bone (b), ingrown callus (c) shows a significant level of integration with new bone formation filling the gaps between the struts (Mag 50X). D) A higher magnification of a different region (Mag 200X). (E)–(F): SEM and EDS of the interface of the implant and the native bone. (E) SEM image of the implant, F) EDS showing the distribution various elements of the same area. The elements analyzed and the colors in F are: Calcium (red), Phosphorous (light blue), Oxygen (green), Nitrogen (pink) and Carbon (dark purple). (G)–(H): EDS of the interface of the implant in rabbit femur with ingrown new bone. (G) SEM image of the implant, (H) EDS of the implant site. The PCL-HAp fibers are seen as circular forms (cross sections) while the distribution of various elements is indicated with color. The elements that were analyzed and the colors in B are: calcium (red), phosphorous (light blue), oxygen (green), nitrogen (pink) and carbon (dark purple).

(figures 5(d), (e), (g), (h) and 6(a), (c), (d)). In the longitudinal section of the implant new bone formation was particularly seen around the implant and in the spaces or gaps formed by the struts (figure 7). To quantify the new bone formation, first of all the surrounding muscle and fat tissues and the fibrous connective tissue were cleared and only the newly formed bone tissue was left (figure 5(b)). Then, the percentage of the area of the new bone formed within the entire tissue area (figure 6(a)) was calculated as 24.84%.

In the cross sections of the implant, it was observed that cartilage tissue formation was followed by new bone trabeculae formation as in the endochondral ossification at the periphery of the scaffolds (figure 5(g), (h) and 6 (a), (c)). In addition, there were occasional new bone trabeculae formation between the struts of the scaffold (figure 5(e)). The fibrous connective tissue was especially seen in the spaces between the struts of the scaffold, as well as it was found around the scaffold (figures 5(c), (e) and 6(b)). In the autograft groups, it was observed that there was a sizeable callus formation, and an extensive fibrous connective tissue formation at the defect site (figures 5(i) and (l)). The cartilage tissue and the new bone trabeculae formation through the endochondral ossification were seen also in the autograft group (figures 5(j) and 6(f)). There were new bone trabeculae formations inside and around the autograft tissue, and the intense fibrous connective tissue surrounded this irregularly formed bone tissue (figures 5(i)–(n) and 6(e)–(h)). In both longitudinal and cross sections of the autograft group, a significant amount of foreign body giant cells and macrophages were observed (figures 5(k), (m) and 6(g), (h)). As a consequence, the histological evaluations of both the 3DP PCL-nHAp implant and autograft groups showed that on week 6 of implantation, the fibrocartilaginous callus slowly started to be replaced by the bony callus through endochondral ossification and new bone tissue formations were present.

3.7. Radiographic union score in tibial fracture (RUST) for healing levels

The ICC scores of all sample measurements obtained via RUST evaluation by two observers demonstrated a perfect agreement (ICC = 0.973, 0.952 < ICC < 0.985, %95 CI, $p < 0.001$). When the implant and autograft groups were examined, no significant difference was observed between the two groups within Week 1 ($p = 0.197$, $p > 0.05$) and Week 3 ($p = 0.207$, $p > 0.05$), however, for Week 6 ($p = 0.018$, $p < 0.05$) there was a significant difference with a 95% CI in favor of autograft (figure 8(A)). An increase in the mRUST score was observed for both groups from the start of the experiment to its termination at Week 6. According to these observations overall regression results were statistically significant for both the autograft ($R^2 = 0.90$, $F(1, 22) = 197.43$, $p < 0.000$) and the implant ($R^2 = 0.94$, $F(1, 22) = 355.01$ $p < 0.000$) groups with a 95% CI (figure 8(B)).

3.8. CT volume analysis

No significant volume difference was observed between the autograft and implant groups ($p = 0.1205$, $p > 0.05$) (figure 8(C)). There is a statistically significant difference between the Autograft-Control ($p = 0.000$, $p < 0.001$) and Implant-Control ($p = 0.008$, $p < 0.01$) groups according to the comparison of the volumes (mm^3) in the spaces that occupied between the parallel planes leaving a 20 mm gap.

3.9. Macroscopic findings

The surgical fixation of fractured extremities with hardware is necessary to prevent movement between the implant and the bone endings. In this study, a K-wire was used to fixate each autograft and implant to the adjacent native bone tissue. The implant was pierced in the middle by the K-wire and this provided a tight grip around the K-wire, improving the fixation of the implant to the native bone. The same K-wire was also used with the autografts and this time it passed through the intramedullar cavity of the native bone. However, since the K-wire was smaller than the intramedullar cavity of the autologous bone, the autografts were held loosely, leading to a less tight fixation of the autograft to the native bone than that of the implant. Thus, the bone healing in the autologous group resulted in varying degrees of bone healing, causing a high standard deviation in the results of the 3-point bending test.

During segmental bone graft implantation at a segmental bone defect, PCL-nHAp implant provided more stability at time zero compared to segmental bone autograft and made the procedure easier for intramedullary K-wire placement needed for the stabilization of the graft due to its dense multifiber nature which allowed more stability.

According to figure 9(A), healing process could be observed during the experiment to score radiologically. At the end of the experiment, K-wires were pulled out to create more reliable 3D reconstructions with precise volume analysis (figure 9(B)). Macroscopic findings of the bone defect area before biomechanical testing showed that there was neither a healing deficit nor macroscopic motion at the segmental defect area after removal of intramedullary K-wires from the femurs in both (autologous and implant) groups (figure 9(B)). An important point is that in the lateral 3D reconstructions the implant is not seen because the implant is constructed of a polymeric material which is invisible when viewed with x-rays.

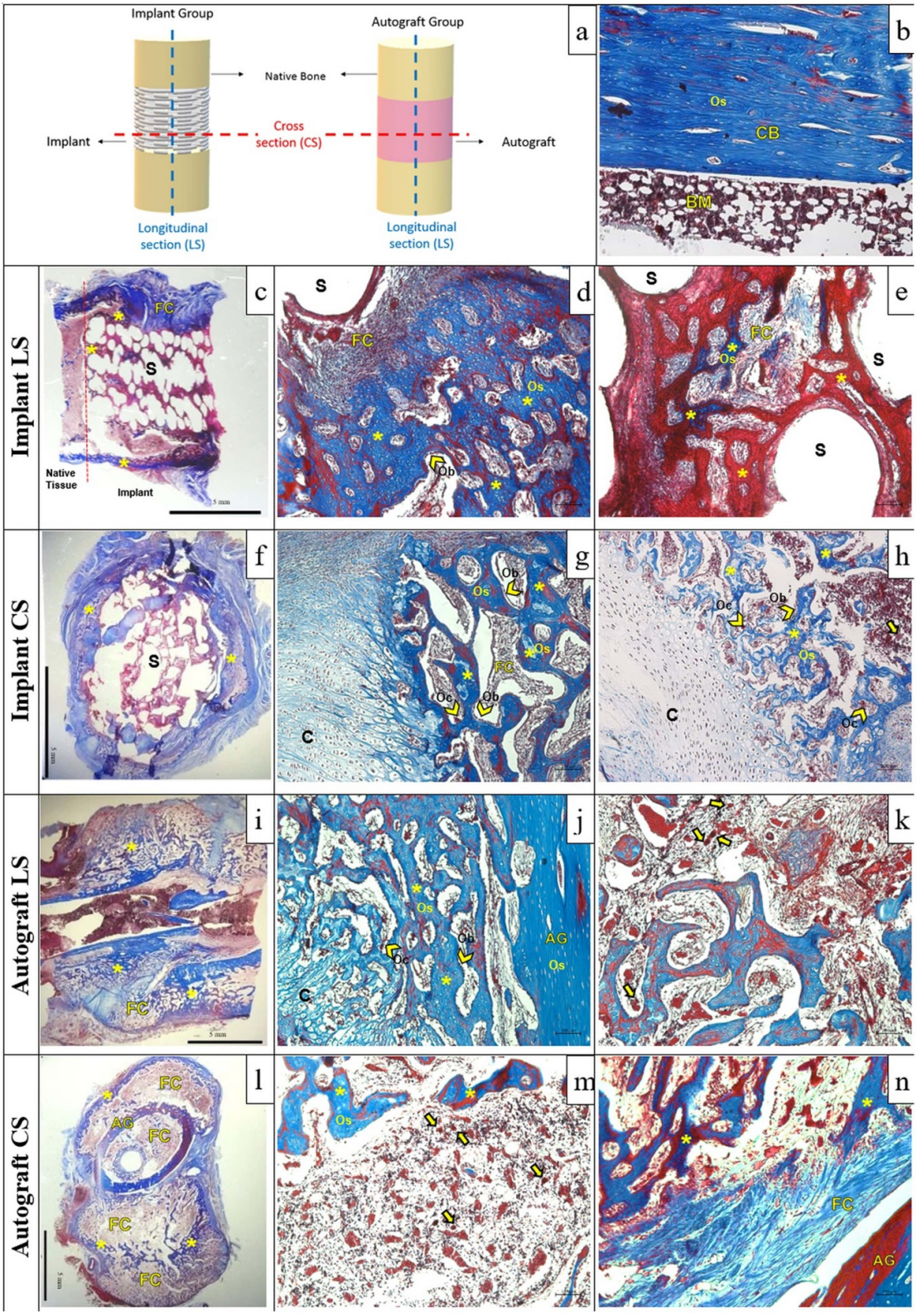

Figure 5. Histological evaluation of *in vivo* bone tissue regeneration after 6 weeks of implantation following Masson's trichrome staining. (a) Schematic illustration of longitudinal section (LS) and cross section (CS) of the implant and the autograft samples. (b) Light microscope image of control bone tissue. Stereomicrographs of (c), (f) the implants and (i), (l) the autografts, scale bar: 5 mm. Analysis of (d), (e), (g), (h) the implants and (j), (k), (m), (n) the autografts by light microscopy, scale bar: 100 μm. (* denotes new bone formation, arrow heads indicate osteoblast and osteoclasts, arrows indicate foreign body giant cells and macrophages, FC: fibrous connective tissue, C: cartilage tissue, S: scaffold strut, AG: autograft, BM: bone marrow, CB: compact bone, Ob: osteoblasts, Os: osteocytes, Oc: osteoclasts).

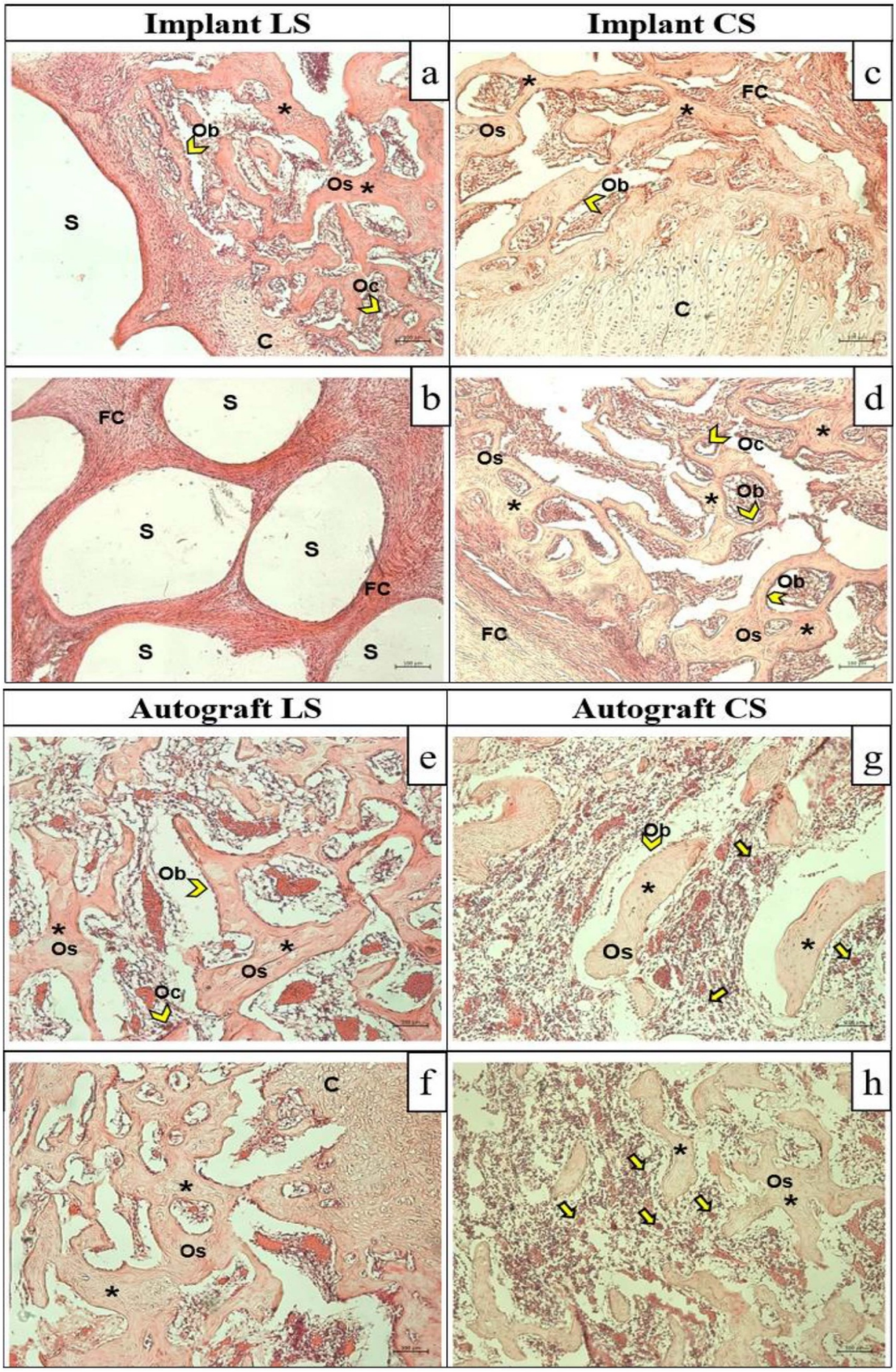

Figure 6. Histological evaluation of *in vivo* bone tissue regeneration after 6 weeks of implantation following H&E staining. Longitudinal section (LS) and cross section (CS) of (a)–(d) the implant and (e)–(h)) the autografts by light microscopy, scale bar: 100 μm (* denotes new bone formations, arrow heads indicate osteoblasts and osteoclasts, arrows indicate foreign body giant cells and macrophages, FC: fibrous connective tissue, C: cartilage tissue, S: scaffold strut, Ob: osteoblast, Os: osteocyte, Oc: osteoclast).

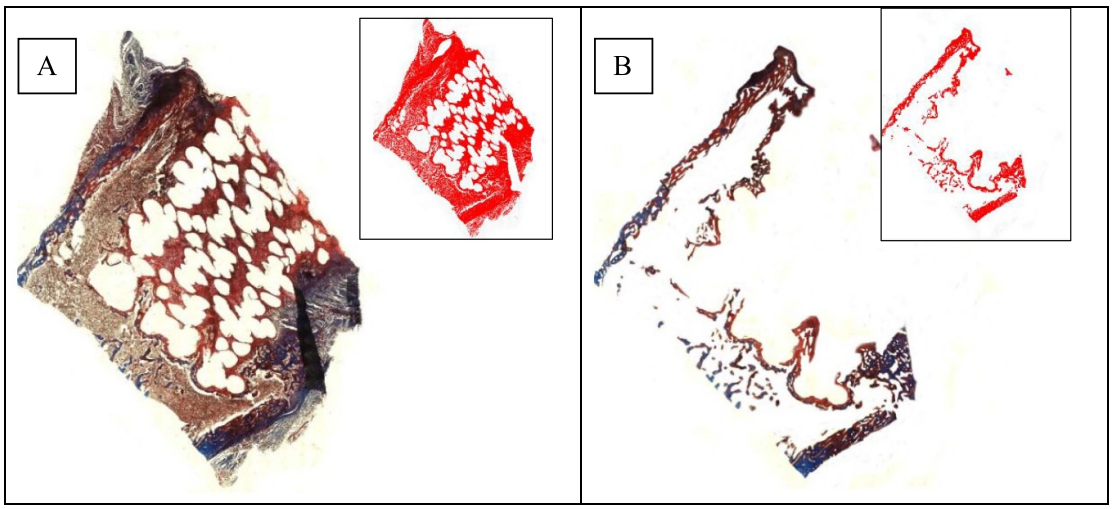

Figure 7. Histological evaluation for new bone formation of *in vivo* bone tissue regeneration after 6 weeks of implantation following Masson's trichrome staining. (A) Tiles image of longitudinal section, (B) Tiles image of the longitudinal section after the surrounding muscle and fat tissues and the fibrous connective tissue were cleared, leaving only the newly formed bone tissue visible. Inserts display the areas where the entire image was converted to a single-channel color for area calculation. (The folds and undefined regions were excluded.).

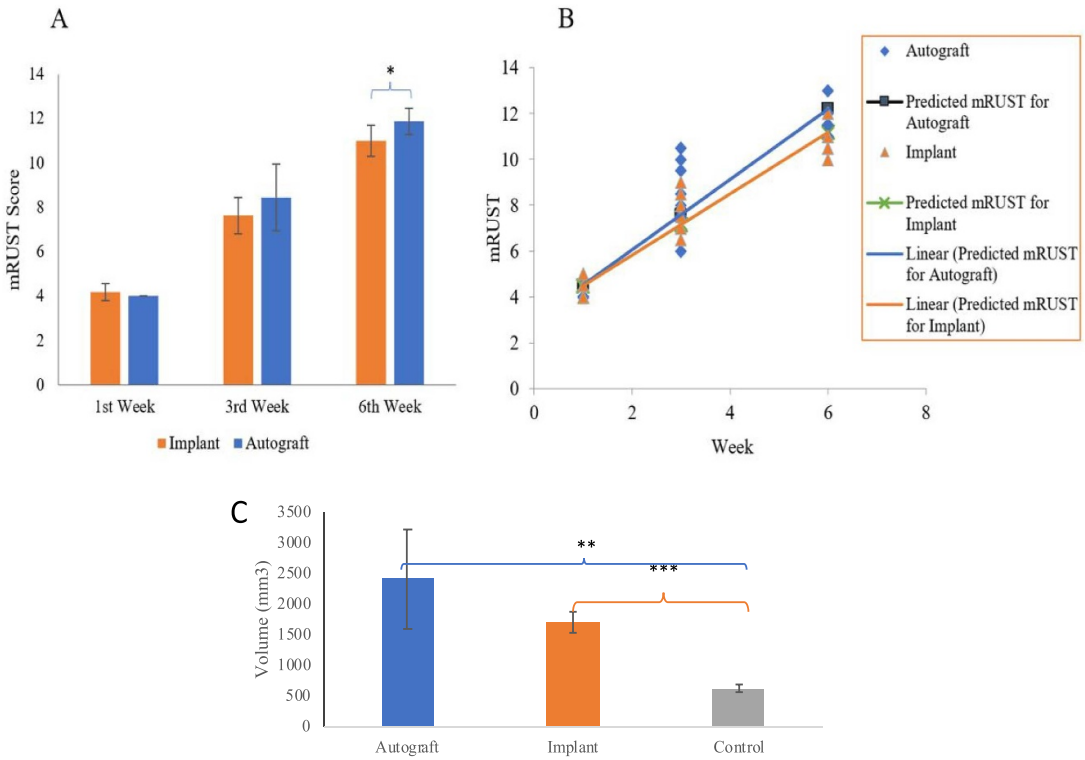

Figure 8. Results of implants and autographs. (A) mRUST results at weeks 1, 3 and 6 after surgery. '*' means that there is a significant difference. (B) Linear regression plot of mRUST score with time. $R^2 = 0.90$ for autograft group and $R^2 = 0.94$ for implant group. C) CT segmented volume graph (week 6). Graph shows the mean values of segmented 20 mm compartment volume with SD. '*', '**' and '***' respectively indicate the following values in terms of statistical significance difference between control group and the others: $p < 0.05$, $p < 0.01$ and $p < 0.001$.

Biomechanical stability at a fracture site can be observed even in the absence of complete radiological union for several reasons:

1) Callus formation: Early in the healing process, a fracture site develops a callus, which is new bone growth [57]. Even if this callus is not fully mineralized or visible on x-rays as a solid union, it can still provide structural support and stability to the fracture site [58].

2) Fibrous healing: In some cases, especially with certain types of fractures or if the fracture is not perfectly aligned, fibrous tissue forms around the

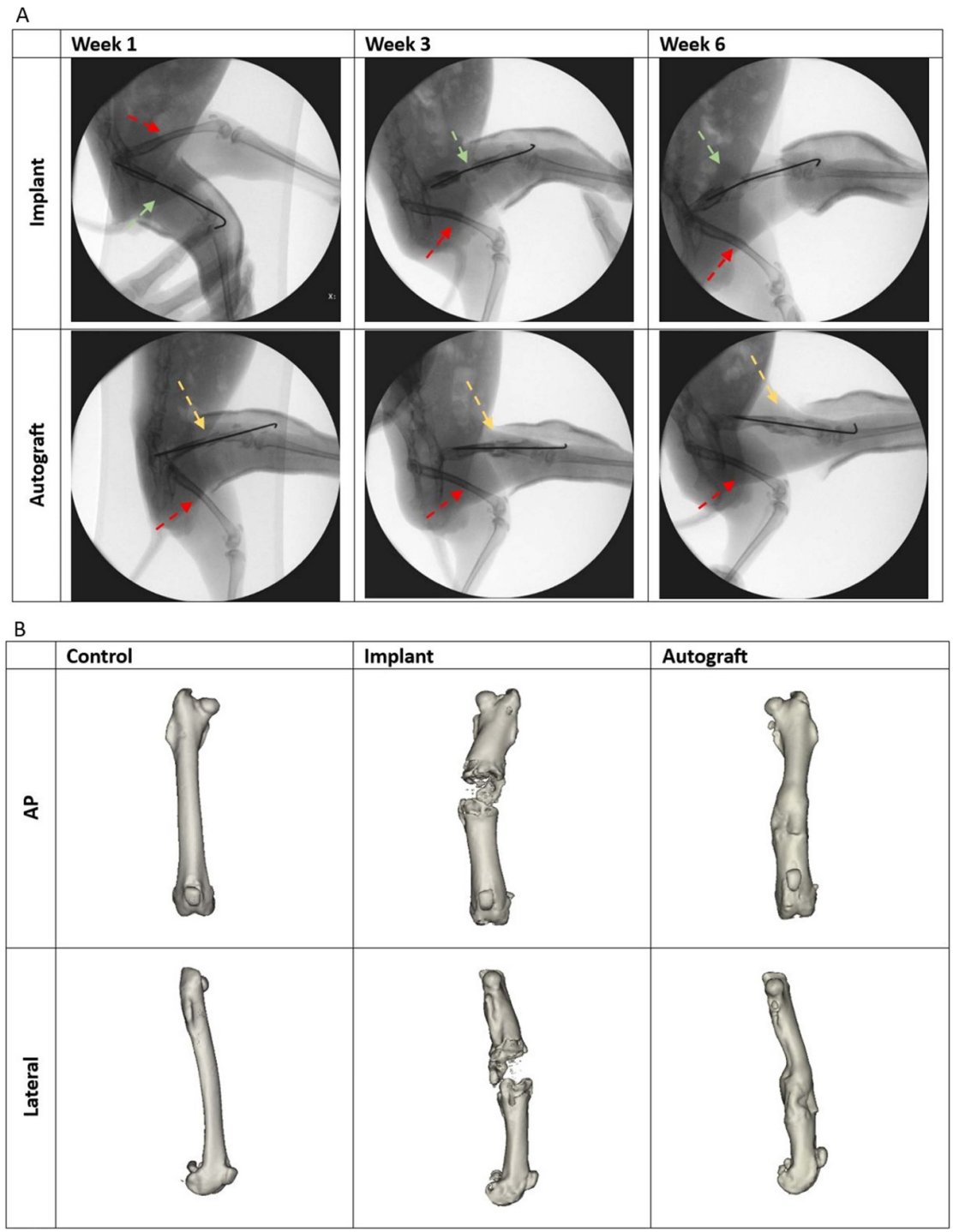

Figure 9. Examples of radiological evaluation of groups with both x-ray and 3D reconstructions (after 6 weeks). (A) Lateral x-ray images of the implant (top) and the autograft (bottom) groups that were used to calculate mRUST scores of AP x-ray graphs. Implants are shown with green arrows, autografts are shown with yellow arrows, and control legs are shown with red arrows.(B) Anterior and lateral 3D reconstructions of control, implant and autograft groups. MIMICS research (version 21.0.0.406) used to create 3D reconstructions of samples and to calculate mineralized volume.

fracture site. While this fibrous tissue may not show up as a solid bony union on radiographs, it can still contribute to stability [59].

3) Bone remodeling: Bone healing is a dynamic process [57]. The initial stages of healing may involve a significant amount of remodeling where the bone structure is reorganized. This remodeling phase might not be fully captured on early x-rays but can still offer biomechanical stability [58]

4. Discussion

Critical sized bone defects are defined as a loss of bone greater than twice the diameter of a long bone

and cannot heal spontaneously over the course of the lifetime of a patient [60, 61]. They present a significant orthopedic challenge, which can result from trauma, tumor resection or infection. Autograft is the gold standard for the treatment of critical-sized bone defects, but it has issues such as limited source, secondary operation, infection risk and donor site morbidity [62]. A synthetic or natural biodegradable device with adequate mechanical properties can be used to overcome these limitations. In this study, the effectiveness of a 3D printed (produced by additive manufacturing), biodegradable implant in treating critical sized segmental bone defects in a rabbit model was assessed. The results of treatment with a 3D printed, biodegradable implant was compared with those of an autograft and a control group. A sham group was not included because critical sized bone defects do not heal spontaneously. The findings of the study were analyzed to compare the performance of the biodegradable implant over the current standard of care approach and to identify its potential advantages over this gold standard.

During the self repair of bone tissue after fracture, dense connective tissue and cartilage tissue form a fibrocartilaginous callus, and then the newly formed bone extends to the surface of the fibrocartilaginous callus [63]. Afterwards, new bone formation from the periphery towards the inside of the callus occurs and this fibrocartilaginous callus is then replaced with bony callus. Finally, spongy bone undergoes remodeling and compact bone is formed.

Similar to the self regeneration process of bone tissue, the histological results of this study showed that new bone trabeculae formations were seen mainly around the implant and the autograft after the 6 weeks of implantation. In addition, the interiors of the implant and autograft were mainly filled with fibrous connective tissue, and new bone trabeculae formations were occasionally observed in the cavities. In this study the mainly hollow biodegradable implant was filled with the ingrowing new tissue while the autograft was already a full, mature, healthy bone section. During bone repair, osteoblasts, the bone precursor cells, are involved in production of new bone matrix, and these cells are differentiated into osteocytes that are entrapped within the mineralized bone matrix [64]. In bone remodeling, osteoclasts resorb bone tissue and osteoblasts synthesize new bone tissue. In histological images of both implant and autograft groups, it was observed that osteoblasts surrounded the newly developed trabeculae and osteoclasts were occasionally seen in the cavities at the periphery, while the osteocytes were entrapped within newly formed trabeculae. Consequently, the histological results of both the implant and the autograft indicated that, as in the process of bone self-repair, the replacement of the fibrocartilaginous callus by a bony callus occurred through endochondral ossification and the formation of new bone tissue began [65, 66]. It was also reported that biomaterials that allow cell attachment and differentiation, promote bone formation through endochondrial ossification pathway [67, 68]

SEM micrographs also showed that this biodegradable device produced by 3D printing of a PCL polymer allowed tissue ingrowth. The most important finding of the study is that the biodegradable cylindrical implant constructed with nano HAp carrying PCL polymer struts (or fibers) successfully substituted for the autograft in repairing the segmental femoral bone defect created in rabbit legs. Although the mechanical strength of the biodegradable implant was lower than the autograft, it still had some degree of ultimate load bearing strength at the end of 6 weeks indicating that there was a certain level of integration of the implant had happened (ultimate strength for the implant was 57 ± 5 N and 93 ± 56 N for the autograft) and new bone was produced during the post operational period as was also shown by the histological and SEM results.

The distance between the distal and proximal bone fractures during bone healing affects the healing of the callus tissue as either non-critical or critical [69]. According to this, the formation of callus tissue by bone tissue, even if the distance increases, undergoing non-critical healing is a condition that one would like to observe clinically. mRUST analyses showed that both groups had comparable radiological healing level. At time zero, during the internal fixation process, 3D printed PCL-HAp implant showed higher stability due its strong, load bearing structure and design. The 3D printing approach which created criss cross patterned gaps between struts was instrumental in tissue ingrowth and as a result permitted to better interaction between the polymer and the ingrowing cartilage tissue. The results of this study indicate that both groups have non-critical bone healing around the defected area.

The mRUST analysis also showed that both groups exhibited non-critical bone healing around the defected area. Despite the fact that the difference between groups at week 6 was significant, this result proves us that healing process of the implant takes more time than that of the autograft but without interrupting the non-critical healing, especially when this situation is considered together with the linear regression results of the implant group. Moreover, in week 6 no significant difference can be observed in the volumes of the autograft and implant groups, indicating that both treatments are actively involved in the mineralization of the defect site. All of these suggest that the implant can be used for bone healing in large

defects. Besides, 3D printed PCL-HAp implant offers the capability of being patient specific if printed based on a MR or similar data of the defect site [70].

Overall, it seems to be comparable to autogenic segmental femoral bone graft in terms of both bone healing and biomechanical stability which appears to be a viable option for large segmental bone defects where there is limited amount of natural autogenic bone grafting availability.

Future studies need to be continued to investigate the long term efficacy and safety of this implant in the treatment of bone defects. The weakness in mechanical strength can lead to re-fractures during the healing process. Therefore, in this study, a Kirschner-wire was used to maintain mechanical stability for cylindrical implant, which mimicked the clinically used intramedullary nail. In order to obtain more stability, the removal time of the relevant instruments should be extended compared with routine treatment protocol. In the present study even though, satisfactory results were obtained at the end of the 6 weeks of implantation, it can be stated that an observation period of 3–6 months would be more appropriate during which remodulation and healing phases of bone can be observed and evaluated. The results of this study provide promising evidence for the use of the biodegradable 3D printed PCL-HAp implant as an alternative to autograft in the treatment of large segmental bone defects. This could have significant implications in improving patient outcomes and reducing the need for autogenic bone grafting, which can be limited in availability and associated morbidity.

5. Conclusion

Biodegradable, 3D printed PCL-HAp implant has shown promising results as an alternative to autografts in the treatment of large segmental bone defects. The implant was able to overcome the need for bone grafting and exhibit comparable bone healing and biomechanical stability with autograft. The tissue ingrowth and integration with the bone, as well as the radiological measurements taken over a period of 6 weeks, suggest that this implant could be a useful option for the treatment of bone defects. Overall, the 3D printed biodegradable cylindrical implant offers a potential solution to common challenges in the field of orthopedic surgery.

Data availability statement

The data that support the findings of this study are available upon reasonable request from the authors.

Acknowledgment

The authors would like to acknowledge Acibadem University Biomaterials Center and, Middle East Technical University Center of Excellence in Biomaterials and Tissue Engineering, BIOMATEN, for the use of the facilities.

Ethical committee

Acibadem University ACU-HADYEK (Animal Experiments Local Ethics Committee) approval No: 2018/42 dated 11.10.2021 was obtained for the project titled ‘Kemik defektlerinin tedavisinde kullanılması planlanan PCL/HAp greftin kaynama bakımından otojen kemik grefti ile katılaştırılması (Translation: Comparison of PCL/HAp graft planned to be used in the treatment of bone defects with autogeneous bone graft from the point of view of fusion)’.

ORCID iDs

D Basoz https://orcid.org/0000-0002-4344-4053
M I Karaman https://orcid.org/0000-0002-7145-1867
N Hasirci https://orcid.org/0000-0002-4497-0194
V Hasirci https://orcid.org/0000-0002-3698-8861

References

[1] Norris B L, Vanderkarr M, Sparks C, Chitnis A S, Ray B and Holy C E 2021 Treatments, cost and healthcare utilization of patients with segmental bone defects *Injury* **52** 2935–40
[2] Pneumaticos S G, Triantafyllopoulos G K, Basdra E K and Papavassiliou A G 2010 Segmental bone defects: from cellular and molecular pathways to the development of novel biological treatments *J. Cell Mol. Med.* **14** 2561–9
[3] Woon C Y-L, Chong K-W and Wong M-K 2010 Induced membranes—a staged technique of bone-grafting for segmental bone loss: a report of two cases and a literature review *JBJS* **92** 196–201
[4] Feltri P, Solaro L, Errani C, Schiavon G, Candrian C and Filardo G 2023 Vascularized fibular grafts for the treatment of long bone defects: pros and cons. A systematic review and meta-analysis *Arch. Orthop. Trauma Surg.* **143** 29–48
[5] Mauffrey C, Barlow B T and Smith W 2015 Management of segmental bone defects *J. Am. Acad. Orthop. Surg.* **23** 143–53
[6] Guda T, Walker J A, Pollot B E, Appleford M R, Oh S, Ong J L and Wenke J C 2011 *In vivo* performance of bilayer hydroxyapatite scaffolds for bone tissue regeneration in the rabbit radius *J. Mater. Sci., Mater. Med.* **22** 647–56
[7] Korn P *et al* 2020 3D printing of bone grafts for cleft alveolar osteoplasty–*in vivo* evaluation in a preclinical model *Front. Bioeng. Biotechnol.* **8** 217
[8] Hong Y R, Kim T-H, Lee K, Lim J O and Oh C-W 2023 Bioactive bone substitute in a rabbit ulna model: preclinical study *Tissue Eng. Regener. Med.* **20** 1205–17
[9] Astudillo Potes M D, Mitra I, Hanson K, Camilleri E T, Gaihre B, Shafi M, Hamouda A, Lu L and Elder B D 2024 Biodegradable poly (caprolactone fumarate) 3D printed scaffolds for segmental bone defects within the Masquelet technique *J. Orthop. Res.* **42** 1974–83

[10] Oladele I O, Omotosho T F and Adediran A A 2020 Polymer-based composites: an indispensable material for present and future applications *Int. J. Polym. Sci.* **2020** 1–12
[11] Wongsupa N, Nuntanaranont T, Kamolmattayakul S, Thuaksuban N and Grijpma D W 2017 Assessment of bone regeneration of a tissue-engineered bone complex using human dental pulp stem cells/poly (ε-caprolactone)-biphasic calcium phosphate scaffold constructs in rabbit calvarial defects *J. Mater. Sci., Mater. Med.* **28** 1–14
[12] Chen X, Gao C, Jiang J, Wu Y, Zhu P and Chen G 2019 3D printed porous PLA/nHA composite scaffolds with enhanced osteogenesis and osteoconductivity *in vivo* for bone regeneration *Biomed. Mater.* **14** 065003
[13] Shim J-H, Yoon M-C, Jeong C-M, Jang J, Jeong S-I, Cho D-W and Huh J-B 2014 Efficacy of rhBMP-2 loaded PCL/PLGA/β-TCP guided bone regeneration membrane fabricated by 3D printing technology for reconstruction of calvaria defects in rabbit *Biomed. Mater.* **9** 065006
[14] Kim J Y *et al* 2010 Evaluation of solid free-form fabrication-based scaffolds seeded with osteoblasts and human umbilical vein endothelial cells for use *in vivo* osteogenesis *Tissue Eng.* A **16** 2229–36
[15] Roy T D, Simon J L, Ricci J L, Rekow E D, Thompson V P and Parsons J R 2003 Performance of degradable composite bone repair products made via three-dimensional fabrication techniques *J. Biomed. Mater. Res.* A **66** 283–91
[16] de Lacerda Schickert S, van den Beucken J J, Leeuwenburgh S C and Jansen J A 2020 Pre-clinical evaluation of biological bone substitute materials for application in highly loaded skeletal sites *Biomolecules* **10** 883
[17] Hatt L P, Thompson K, Helms J A, Stoddart M J and Armiento A R 2022 Clinically relevant preclinical animal models for testing novel cranio-maxillofacial bone 3D-printed biomaterials *Clin. Transl. Med.* **12** e690
[18] Yang Y *et al* 2024 3D-printed PCL framework assembling ECM-inspired multi-layer mineralized GO-Col-HAp microscaffold for *in situ* mandibular bone regeneration *J. Transl. Med.* **22** 224
[19] Hou X, Zhang L, Zhou Z, Luo X, Wang T, Zhao X, Lu B, Chen F and Zheng L 2022 Calcium phosphate-based biomaterials for bone repair *J. Funct. Biomater.* **13** 187
[20] Hasirci V and Hasirci N 2018 Ceramics *Fundamentals of Biomaterials* ed V Hasirci and N Hasirci (Springer) pp 51–64
[21] Bansal R, Patil S, Chaubey K K, Thakur R K and Goyel P 2014 Clinical evaluation of hydroxyapatite and β-tricalcium phosphate composite graft in the treatment of intrabony periodontal defect: a clinico-radiographic study *J. Indian Soc. Periodontol.* **18** 610–7
[22] Gao W, Deng J, Ren J, Zhang W, Wang Z, He R, Wang K, Shi X and Liang T 2022 3D-printed hydroxyapatite (HA) scaffolds combined with exos from BMSCs cultured in 3D HA scaffolds to repair bone defects *Composites* B **247** 110315
[23] Mohd N, Razali M, Ghazali M J and Abu Kasim N H 2022 3D-printed hydroxyapatite and tricalcium phosphates-based scaffolds for alveolar bone regeneration in animal models: a scoping review *Materials* **15** 2621
[24] Zhi W *et al* 2022 Optimal regenerative repair of large segmental bone defect in a goat model with osteoinductive calcium phosphate bioceramic implants *Bioact. Mater.* **11** 240–53
[25] Ray B, Oskolkov B, Liu C, Leblanc Z and Tian W 2023 FFF-based metal and ceramic additive manufacturing: production scale-up from a stream of variation analysis perspective *Manuf. Lett.* **35** 811–21
[26] Bogala M 2022 Three-dimensional (3D) printing of hydroxyapatite-based scaffolds: a review *Bioprinting* **28** e00244
[27] Yeo T, Ko Y-G, Kim E J, Kwon O K, Chung H Y and Kwon O H 2021 Promoting bone regeneration by 3D-printed poly (glycolic acid)/hydroxyapatite composite scaffolds *J. Ind. Eng. Chem.* **94** 343–51
[28] Shuai C, Yang W, Feng P, Peng S and Pan H 2021 Accelerated degradation of HAP/PLLA bone scaffold by PGA blending facilitates bioactivity and osteoconductivity *Bioact. Mater.* **6** 490–502
[29] Kim J-W, Shin K-H, Koh Y-H, Hah M J, Moon J and Kim H-E 2017 Production of poly (ε-caprolactone)/hydroxyapatite composite scaffolds with a tailored macro/micro-porous structure, high mechanical properties, and excellent bioactivity *Materials* **10** 1123
[30] Hasirci V and Hasirci N 2018 *Biomaterials and Devices in Hard Tissue Augmentation. Fundamentals of Biomaterials* (Springer) pp 219–32
[31] Gunay B, Hasirci N and Hasirci V 2017 A cell attracting composite of lumbar fusion cage *J. Biomater. Sci. Polym. ed.* **28** 749–67
[32] Barnthip N, Teeka J, Kantha P, Teepoo S and Damjuti W 2022 Fabrication and characterization of polycaprolactone/cellulose acetate blended nanofiber mats containing sericin and fibroin for biomedical application *Sci. Rep.* **12** 22370
[33] Wang S, Gu R, Wang F, Zhao X, Yang F, Xu Y, Yan F, Zhu Y, Xia D and Liu Y 2022 3D-Printed PCL/Zn scaffolds for bone regeneration with a dose-dependent effect on osteogenesis and osteoclastogenesis *Mater. Today Bio* **13** 100202
[34] Buyuksungur S *et al* 2017 3D printed poly (ε-caprolactone) scaffolds modified with hydroxyapatite and poly (propylene fumarate) and their effects on the healing of rabbit femur defects *Biomater. Sci.* **5** 2144–58
[35] Gharibshahian M, Salehi M, Beheshtizadeh N, Kamalabadi-Farahani M, Atashi A, Nourbakhsh M-S and Alizadeh M 2023 Recent advances on 3D-printed PCL-based composite scaffolds for bone tissue engineering *Front. Bioeng. Biotechnol.* **11** 1168504
[36] Wang W, Zhou X, Yin Z and Yu X 2023 Fabrication and evaluation of porous dECM/PCL scaffolds for bone tissue engineering *J. Funct. Biomater.* **14** 343
[37] Yilgor P, Sousa R A, Reis R L, Hasirci N and Hasirci V (eds) 2008 3D plotted PCL scaffolds for stem cell based bone tissue engineering *Macromolecular Symposia* (Wiley)
[38] Isik G, Kiziltay A, Hasirci N and Tezcaner A 2022 Lithocholic acid conjugated mPEG-b-PCL micelles for pH responsive delivery to breast cancer cells *Int. J. Pharm.* **621** 121779
[39] Sezer U A, Aksoy E A, Hasirci V and Hasirci N 2013 Poly (ε-caprolactone) composites containing gentamicin-loaded β-tricalcium phosphate/gelatin microspheres as bone tissue supports *J. Appl. Polym. Sci.* **127** 2132–9
[40] Bosworth L A and Downes S 2010 Physicochemical characterisation of degrading polycaprolactone scaffolds *Polym Degrad. Stab.* **95** 2269–76
[41] Malikmammadov E, Tanir T E, Kiziltay A, Hasirci V and Hasirci N 2018 PCL-TCP wet spun scaffolds carrying antibiotic-loaded microspheres for bone tissue engineering *J. Biomater. Sci. Polym. Ed.* **29** 805–24
[42] Sezer U A, Billur D, Huri G, Huri P Y, Aksoy E A, Terzioglu H, Konukseven E, Hasirci V and Hasirci N 2014 *In vivo* performance of poly (ε-caprolactone) constructs loaded with gentamicin releasing composite microspheres for use in bone regeneration *J. Biomater. Tissue Eng.* **4** 786–95
[43] Eftekhari H, Jahandideh A, Asghari A, Akbarzadeh A and Hesaraki S 2017 Assessment of polycaprolacton (PCL) nanocomposite scaffold compared with hydroxyapatite (HA) on healing of segmental femur bone defect in rabbits *Artif. Cells Nanomed. Biotechnol.* **45** 961–8
[44] Yilgor P, Yilmaz G, Onal M B, Solmaz I, Gundogdu S, Keskil S, Sousa R A, Reis R L, Hasirci N and Hasirci V 2013 An *in vivo* study on the effect of scaffold geometry and growth factor release on the healing of bone defects *J. Tissue Eng. Regener. Med.* **7** 687–96
[45] Huang W, Cai X, Xiao C, Song W, Yin H and Xu W 2024 Surface micropatterning of 3D printed PCL scaffolds promotes osteogenic differentiation of BMSCs and regulates macrophage M2 polarization *Heliyon* **10** e26621

[46] Park H, Choi J W and Jeong W S 2022 Clinical application of three-dimensional printing of polycaprolactone/beta-tricalcium phosphate implants for cranial reconstruction *J. Craniofac. Surg.* **33** 1394–9
[47] Mayfield C K, Ayad M, Lechtholz-Zey E, Chen Y and Lieberman J R 2022 3D-Printing for critical sized bone defects: current concepts and future directions *Bioengineering* **9** 680
[48] Kon E *et al* 2021 Bone regeneration in load-bearing segmental defects, guided by biomorphic, hierarchically structured apatitic scaffold *Front. Bioeng. Biotechnol.* **9** 734486
[49] Popkov A, Kononovich N, Dubinenko G, Gorbach E, Shastov A, Tverdokhlebov S and Popkov D 2023 Long bone defect filling with bioactive degradable 3D-Implant: experimental study *Biomimetics* **8** 138
[50] Fisher J S, Kazam J J, Fufa D and Bartolotta R J 2019 Radiologic evaluation of fracture healing *Skel. Radiol.* **48** 349–61
[51] Whelan D B, Bhandari M, Stephen D, Kreder H, McKee M D, Zdero R and Schemitsch E H 2010 Development of the radiographic union score for tibial fractures for the assessment of tibial fracture healing after intramedullary fixation *J Trauma Acute Care Surg.* **68** 629–32
[52] Plumarom Y, Wilkinson B G, Willey M C, An Q, Marsh L and Karam M D 2021 Sensitivity and specificity of modified RUST score using clinical and radiographic findings as a gold standard *Bone Joint Open* **2** 796–805
[53] Litrenta J *et al* 2015 Determination of radiographic healing: an assessment of consistency using RUST and modified RUST in metadiaphyseal fractures *J. Orthop. Trauma* **29** 516–20
[54] Landis J R and Koch G G 1977 The measurement of observer agreement for categorical data. biometrics pp 159–74 (available at: https://wwww.jstor.org/stable/2529310)
[55] Nam J H, Lee S Y, Khan G and Park E S 2020 Validation of the optimal scaffold pore size of nasal implants using the 3-dimensional culture technique *Arch. Plast. Surg.* **47** 310–6
[56] Abbasi N, Hamlet S, Love R M and Nguyen N-T 2020 Porous scaffolds for bone regeneration *J. Sci.* **5** 1–9
[57] Ghiasi M S, Chen J, Vaziri A, Rodriguez E K and Nazarian A 2017 Bone fracture healing in mechanobiological modeling: a review of principles and methods *Bone Rep.* **6** 87–100
[58] Liu Q, Liu Z, Guo H, Liang J and Zhang Y 2022 The progress in quantitative evaluation of callus during distraction osteogenesis *BMC Musculoskelet. Disord.* **23** 490
[59] Buckwalter J A and Grodzinsky A J 1999 Loading of healing bone, fibrous tissue, and muscle: implications for orthopaedic practice *J. Am. Acad. Orthop. Surg.* **7** 291–9
[60] Roddy E, DeBaun M R, Daoud-Gray A, Yang Y P and Gardner M J 2018 Treatment of critical-sized bone defects: clinical and tissue engineering perspectives *Eur. J. Orthop. Surg. Traumatol.* **28** 351–62
[61] Bezstarosti H, Metsemakers W-J, Van Lieshout E, Voskamp L, Kortram K, McNally M, Marais L C and Verhofstad M H J 2021 Management of critical-sized bone defects in the treatment of fracture-related infection: a systematic review and pooled analysis *Arch. Orthop. Trauma Surg.* **141** 1215–30
[62] Wang W and Yeung K W 2017 Bone grafts and biomaterials substitutes for bone defect repair: a review *Bioact. Mater.* **2** 224–47
[63] Ross M H and Pawlina W 2006 *Histology: A Text and Atlas: With Correlated Cell and Molecular Biology* vol xvii, 5th edn(Lippincott Wiliams & Wilkins) p 906
[64] Rentsch C, Schneiders W, Manthey S, Rentsch B and Rammelt S 2014 Comprehensive histological evaluation of bone implants *Biomatter* **4**
[65] Sheen J R, Mabrouk A and Garla V V 2023 *Fracture Healing Overview* (StatPearls Publishing)
[66] ElHawary H, Baradaran A, Abi-Rafeh J, Vorstenbosch J, Xu L and Efanov J I (eds) 2021 Bone healing and inflammation: principles of fracture and repair *Seminars in Plastic Surgery* (Thieme Medical Publishers, Inc)
[67] Wei S, Ma J-X, Xu L, Gu X-S and Ma X-L 2020 Biodegradable materials for bone defect repair *Milit. Med. Res.* **7** 1–25
[68] Petersen A *et al* 2018 A biomaterial with a channel-like pore architecture induces endochondral healing of bone defects *Nat. Commun.* **9** 4430
[69] Hoerth R M, Seidt B M, Shah M, Schwarz C, Willie B M, Duda G N, Fratzl P and Wagermaier W 2014 Mechanical and structural properties of bone in non-critical and critical healing in rat *Acta Biomater.* **10** 4009–19
[70] Hollister S J, Flanagan C L, Morrison R J, Patel J J, Wheeler M B, Edwards S P and Green G E 2016 Integrating image-based design and 3D biomaterial printing to create patient specific devices within a design control framework for clinical translation *ACS Biomater. Sci. Eng.* **2** 1827–36